PHILOSOPHICAL TRANSACTIONS OF THE ROYAL SOCIETY A

*Phil. Trans. R. Soc. A* (2005) **363**, 1663–1676
doi:10.1098/rsta.2005.1600
*Published online* 28 June 2005

# Granular ripples under rotating flow: a new experimental technique for studying ripples in non-rotating, geophysical applications?

By P. J. Thomas[1] and F. Zoueshtiagh[2]

[1]*Fluid Dynamics Research Centre, School of Engineering, University of Warwick, Coventry CV4 7AL, UK*
(pjt1@eng.warwick.ac.uk)
[2]*Laboratoire de Mécanique de Lille, UMR-CNRS 8107 Boulevard Paul Langevin, Cité Scientifique, 59655 Villeneuve d'Ascq, France*

A review of our research investigating a new pattern formation process in granular material underlying a rotating fluid is given. The purpose of this summary is to introduce the phenomenon to the geophysical research community and to draw attention to the potential practical benefits of our new experimental method. To this end, the applied and scientific advantages of the technique over traditional studies employing, for instance, water channels, are discussed for the first time. It is shown here that the system rotation in our new technique does not appear to affect the scaling law expressing the dependence of the ripple-pattern wavelength on the governing independent experimental parameters. This suggests that it may become possible to extrapolate appropriate results from rotating to non-rotating systems and, hence, to geophysical environments. Consequently, our new technique may find applications in the context of geophysical research on the formation of sedimentary granular ripple structures.

**Keywords: fluid dynamics; granular flows; pattern formation; sand ripples**

## 1. Introduction

Geophysical systems where a gas or a liquid flows over an underlying expanse of loose, granular material can display the formation of characteristic, depositional bedforms known as sand ripples. Modern studies investigating these patterns and the associated physical mechanisms leading to their formation originate with the seminal work of Bagnold (1941). Fundamental aspects relating to the subject and the research developments in the field were summarized by, for instance, Allen (1984), Sleath (1984), Raudkivi (1990), Lancaster (1995) and Blondeaux (2001).

Air-flow- and liquid-flow-induced ripple patterns differ from one another and they are classified as aeolian and fluvial ripples, respectively. In general, however, sand ripples typically comprise relatively small-scale features composed of fine-grained sand particles with diameters around or below 1 mm. The ripples have a wavy, often asymmetric, cross-sectional surface profile and they are

One contribution of 11 to a Theme 'Geophysical granular and particle-laden flows'.

usually aligned transversely to the flow direction. The typical ripple wavelength ranges between a few millimetres and several tens of centimetres with associated maximum amplitudes up to about a few centimetres (Bagnold 1941; Allen 1984; Sleath 1984; Raudkivi 1990; Lancaster 1995). Ripple-pattern characteristics are usually non-stationary; their cross-section profile and their wavelength have, for instance, been observed to evolve with time (Raudkivi 1997; Stegner & Wesfreid 1999).

Owing to the large variety of different patterns observed, there does not, however, exist a commonly accepted, unique definition of what, in fact, constitutes a sand ripple. Lancaster (1995) points out, for instance, that Sharp (1963) and Fryberger *et al.* (1992) discuss aeolian structures composed of coarse sand or granules with median sizes in the range 1–4 mm, wavelengths as long as 0.5–2 m and amplitudes of 0.1 m or more and they refer to them as granule ripples, or as megaripples in the case of Greeley & Iversen (1985). Various other terminologies have been introduced in attempts to classify patterns according to their appearance or their anticipated physical origins (Sleath 1984). Nevertheless, many details of the physical mechanisms resulting in the different types of ripple patterns are not yet understood.

Well-known examples of aeolian ripples are those ripples observed in deserts while typical fluvial ripples are encountered on the bottom of the ocean or on beaches. Evidently, the formation of ripples necessitates that the granular material is set in motion by the flow above it. Consequently, the ripple-formation process is closely associated with environmental issues such as soil erosion or sediment transport by streams and rivers, as well as with industrial applications including, for instance, materials handling. The literature on the subject is vast and, as Raudkivi (1990) points out, it is scattered in publications and reports in which the emphasis varies according to the area of interest. New results appear, for instance, in the contexts of sedimentology, palaeontology, mineralogy, oceanography, coastal sedimentary environments, geography, agriculture, civil engineering or mining.

The present study is concerned with the early stages in the formation of fluvial ripples. Laboratory studies investigating aspects associated with such ripples often employ water channels (e.g. Kennedy & Falcon 1965; Yalin 1965; Harms 1969; Sleath 1976) for this purpose. Water-channel studies can be inconvenient and laborious if large parameter ranges of the governing independent parameters, such as particle size, density and flow velocity, have to be explored. Further, in water channels, influences arising from the presence of the sidewalls of the facility can affect the flow and bias the ripple-formation process. Here we review our results obtained in a new type of system which has advantages over traditional water channels. In our new system, ripples form in a granular matter underlying rotary flow.

The main purpose of this short summary of results is to introduce our new experimental technique in a geophysical context and to draw attention to its potential benefits with regard to laboratory studies on ripple formation in geophysical applications. These practical issues were not discussed or highlighted in our existing publications. Related to this, it will be shown here for the first time that the background rotation of the system does not appear to affect the scaling law expressing the dependence of the ripple-pattern wavelength on the governing independent experimental parameters. It will be argued that the

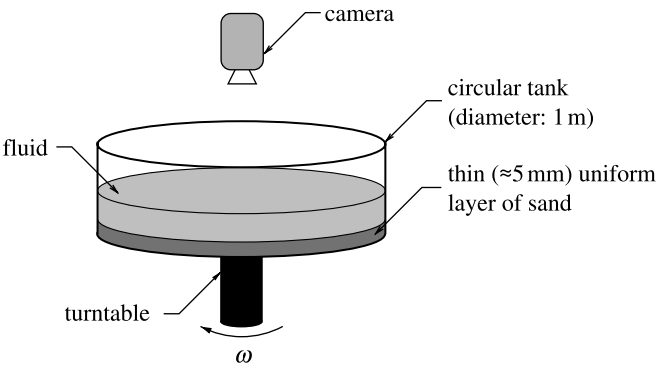


Figure 1. Sketch of the experimental set up.

pattern characteristics at the onset of the formation are determined by the critical shear-stress threshold required to mobilize the particles. The background rotation of the system, which results in Coriolis and centrifugal forces, is essentially irrelevant as regards the granular phase at ripple-formation onset. This suggests that it may be possible to extrapolate and apply results obtained from experiments in the new rotating system to non-rotating systems and, hence, to geophysical environments. The discussion will show that there is experimental evidence that this is in fact the case. Thus, our new experimental technique may not only be relevant to situations involving rotary flow over an expanse of granular material. In the future, it may also reveal itself as a tool greatly simplifying laboratory experiments investigating the formation of sedimentary ripple structures in non-rotating geophysical flows.

## 2. Experimental set up

Our new experimental system is conceptually simple. It constitutes a circular fluid-filled tank (radius $R \approx 0.5$ m) positioned on a rotating turntable. The arrangement is schematically illustrated in figure 1. Prior to the experiment small granules—such as sand—are distributed in a thin uniform layer across the bottom of the tank. The layer thickness is typically between 3 and 30 mm and the grain diameter ranges between $0.11 \leq d_G \leq 3.17$ mm. The tank is then gradually spun up to a rotation rate $\omega_0$. The spin-up process is sufficiently slow to ensure that the granules are not set in motion during this initial, preparatory phase for the subsequent experiment. When the tank has reached the rotation rate $\omega_0$, the system is allowed to rest and adopt a state of solid-body rotation. Once this has been achieved the granules on the bottom of the tank and the fluid above it do not move relative to each other. Then the actual experiment can begin. To this end, the turntable supporting the tank is instantaneously spun up from its initial rotation rate, $\omega_0$, by an increment $\Delta\omega$, to a higher rotation rate, $\omega_1$. The values of $\omega_0$ and $\omega_1$ ranged between 0 rad s$^{-1}$ and 5 rad s$^{-1}$ and, hence, $\Delta\omega = \omega_1 - \omega_0$ was within $0 \text{ rad s}^{-1} < \Delta\omega < 5 \text{ rad s}^{-1}$. Owing to its inertia, the fluid inside the tank cannot follow the instantaneous spin up of the tank, which has the granules resting on its bottom. A fluid boundary layer is established over the loose-boundary granular layer. This results in shear forces

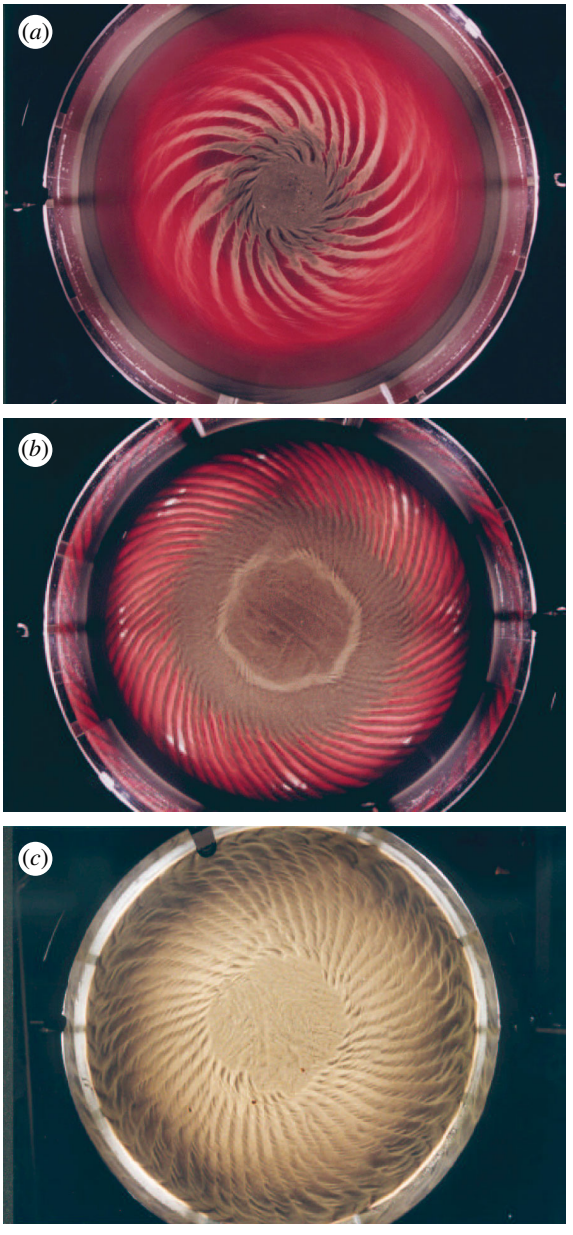


Figure 2. Spiral pattern observed in an experiment with (*a*) $\Delta\omega = 2.15\ \mathrm{rad\,s^{-1}}$, $\omega_1 = 3.16\ \mathrm{rad\,s^{-1}}$ and an initial height of the granule layer of about 5 mm; (*b*) $\Delta\omega = 1.3\ \mathrm{rad\,s^{-1}}$, $\omega_1 = 4.0\ \mathrm{rad\,s^{-1}}$ and an initial height of the granule layer of about 5 mm; and (*c*) $\Delta\omega = 1.02\ \mathrm{rad\,s^{-1}}$, $\omega_1 = 3.54\ \mathrm{rad\,s^{-1}}$ and an initial height of the granule layer of about 30 mm. The turntable is rotating clockwise.

which act on the granules on the surface of the granular layer. If the increment $\Delta\omega$ is sufficiently large, then shear forces become high enough to mobilize these granules. They begin to slide across the bottom of the tank and initiate the ripple-pattern formation process which is the subject of this study.

## 3. Typical ripple patterns generated in the experiment

Typical patterns observed in the experiments are illustrated in figure 2. The patterns are fully formed within 10–20 s of the spin up of the tank. Depending on the experimental conditions, patterns with $7 \leq n \leq 110$ spiral arms originating from a uniform, circular granule patch of radius $r_0$ located in the centre of the tank develop. Granules located inside the patch, i.e. at positions $r < r_0$ remain unaffected by the ongoing re-organization process on its outside. Both $n$ and $r_0$ are independent of time and the data analysis revealed that $n \propto \Delta\omega^{-1}$ and $r_0 \propto \Delta\omega^{-1}$.

The patterns in figure 2*a*,*b* were formed for a thin granule layer with an initial thickness of approximately 5 mm, while figure 2*c* displays a pattern in a thick layer with an initial thickness of approximately 30 mm. For the experiments shown in figure 2*a*,*b*, the initial granule-layer depth was not sufficient to ensure that the bottom of the tank remained completely covered during the pattern formation process. Large areas between successive spiral arms, i.e. at radial locations $r > r_0$, are entirely granule free. When the initial layer depth is sufficiently large, as for the experiment shown in figure 2*c*, then the bottom of the tank remains completely covered with granules after the pattern formation process is completed.

## 4. Computational model

A cellular-automaton model was used to simulate the observed spiral-ripple patterns computationally. A detailed description of the model is contained in Zoueshtiagh & Thomas (2000) and Zoueshtiagh (2001). The simulation is based on the adaptation of a model originally introduced by Nishimori & Ouchi (1993) in the context of modelling ripple formation in a straight-channel geometry.

Briefly, our simulations were performed on a computational grid with Cartesian coordinates $x$, $y$ and $200 \times 200$ grid points. The height of the sand surface at any site $(x_i, y_i)$ is $h(x_i, y_i)$. The computational domain is appropriately initialized to represent the random, unstructured grain height distribution of the granular layer on the bottom of the tank prior to the experiment. Saltation and creep (Bagnold 1941; Nishimori & Ouchi 1993) are assumed to be the two mechanisms responsible for grain transport during the spin-up phase. To model these mechanisms, grains are moved around the computational domain according to simple rules. This results in the distribution $h(x_i, y_i)$ being updated in successive iteration steps. The expressions used to move particles incorporate control parameters representing aspects such as the shear stress imposed on the sand surface by the fluid moving above it or the mean flow velocity experienced by a grain during its saltation flight. For instance, the flight length will be longer the higher its starting point in the computational domain.

Coriolis forces on moving grains can be incorporated by an appropriate term in the expression for the flight length. However, the data analysis has revealed that the model succeeds in reproducing the experimentally determined scalings for the number $n$ of spiral arms and the radius $r_0$ of the inner granule patch for vanishing Coriolis term.

The model does not incorporate effects resulting from quantities such as the grain size, grain density or the grain shape and its surface properties. In the physical system, these quantities are evidently important as regards the absolute value of the developing ripple wavelength. However, the goal of our simulations is not to provide a realistic model suitable to predict the absolute wavelength. The goal of the model is to explain the scalings $n \propto \Delta\omega^{-1}$ and $r_0 \propto \Delta\omega^{-1}$ observed in the experiments. It will be seen that these scalings are independent of the physical characteristics of the grains.

## 5. Computational patterns

Figure 3*a*,*b* display computationally generated patterns for $\Delta\omega = 5$ and $\Delta\omega = 11$, respectively. Here $\Delta\omega$ is specified in arbitrary, non-dimensional units and not in units of rad $\mathrm{s}^{-1}$ as is the case in the experiments. The patterns do not display a spiral structure because the Coriolis term was inactive in both cases. The grey scale in the figures characterizes the height $h(x_i, y_i)$ of the granules at a particular lattice point $(x_i, y_i)$. Light grey identifies ripple crests, while dark grey represents troughs.

Figure 3*a*,*b* shows a decreasing number $n$ of arms for increasing $\Delta\omega$. The arms originate from an inner patch whose radius decreases with increasing $\Delta\omega$. These results are qualitatively consistent with the experimental observations.

## 6. Comparison of computational and experimental results

Figure 4*a*,*b* compares the measured and the computed results for the number $n$ of spiral arms and the radius $r_0$ of the inner granule patch, respectively. The main result expressed by the two figures is that the experimentally observed scalings, which are approximately equal to $n \propto \Delta\omega^{-1.0}$ and $r_0 \propto \Delta\omega^{-1}$ are, essentially, reproduced by the model.

In both cases, experiment and computation differ by an arbitrary constant reflecting the fact that the computational model does not account for physical properties such as, for instance, the grain size or the grain density. Figure 4*a* shows two alternative interpolations of the experimental data points. The dotted line represents a least-squares-fit based on the entire dataset and was originally obtained by Thomas (1994). The solid line represents a power-law fit $r_0 \propto \Delta\omega^{-1.05}$ to the data points within the interval $1 \leq r_0/R \leq 3.5$. It was argued in Thomas (1994) and in Zoueshtiagh & Thomas (2000) that a $\Delta\omega^{-1}$ scaling is to be expected if centrifugal forces are negligible such that the force required for grain mobilization is constant.

Figure 4*b* shows three alternative power-law type interpolations of the computational data points. The purpose of these three alternative fits is to provide some means for evaluating the error associated with the exponent of the $\Delta\omega$ scaling. The dashed line represents a fit, which takes account of all 12 data points. The dotted line and the solid line represent interpolations for which the three and the five lowest values of $\Delta\omega$ were neglected, respectively. The constants of proportionality for the power-law fits are not explicitly stated because they have no physical significance. For further details concerning the comparison of experimental and computational data points, consult Zoueshtiagh & Thomas (2000).

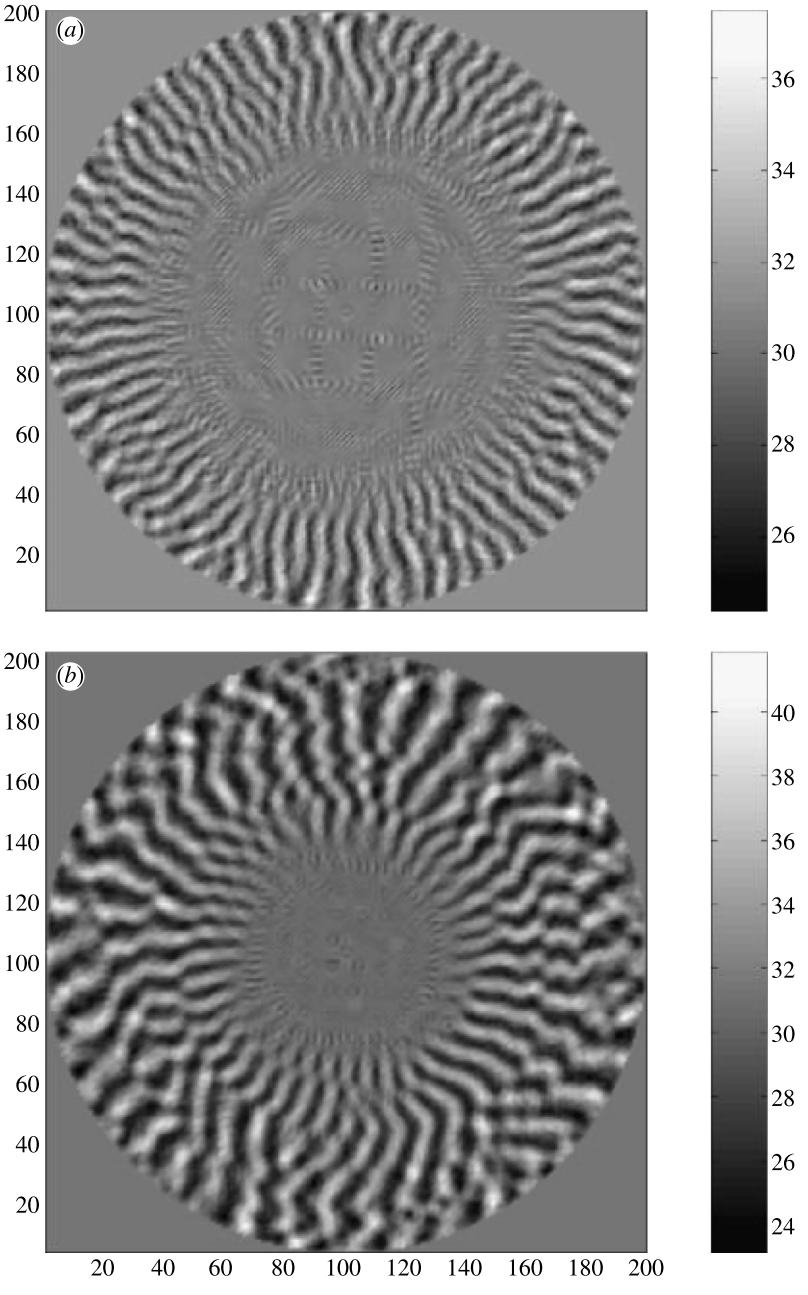


Figure 3. Two computational ripple patterns. The flow speed, $v(r)$, at radius $r$ is $v(r)=\Delta\omega r$, where $\Delta\omega$ is specified in arbitrary units. For the two figures shown, the values of $\Delta\omega$ were (*a*) $\Delta\omega=5$ and (*b*) $\Delta\omega=11$.

The computational model with its simple rules to move grains is, evidently, far too naive to capture the true nature of the complicated interactive dynamics of fluid and granules on the bottom of the tank. Consequently, the agreement of experiment and computation is unlikely to be a consequence of the particular rules specified to

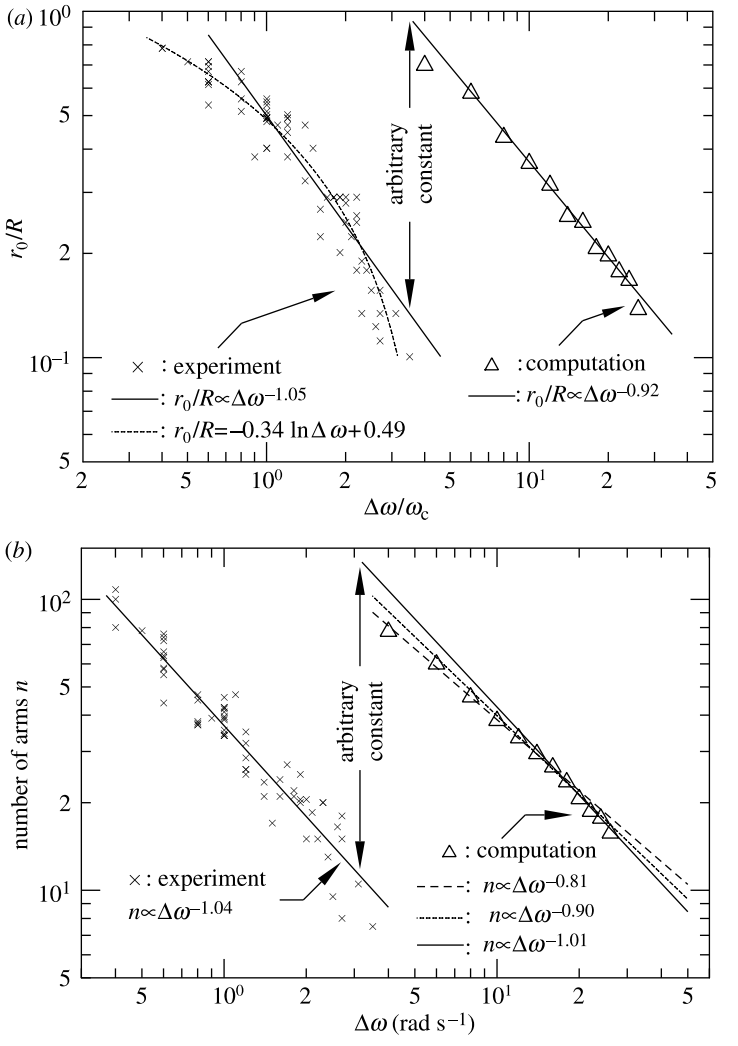


Figure 4. Comparison of experiment and computation for the (*a*) radius $r_0$ of the inner granule patch and (*b*) the number $n$ of ripples developing. In (*a*), the rotational velocity $\omega_c = 1.0$ rad s$^{-1}$, used to non-dimensionalize $\Delta\omega$, is the measured critical velocity that was required for these particular experiments to successfully initiate pattern formation for spin-up from rest, i.e. when $\omega_0 = 0$ and $\omega_1 = 1.0$ rad s$^{-1}$.

move grains across the computational lattice. On the basis of this observation, Zoueshtiagh & Thomas (2000) showed that the scalings arise necessarily as a consequence of the circular geometry in conjunction with the existence of critical onset thresholds for pattern formation in experiment and model. Hence, the rules used to move the grains and, in fact, their motion itself, are irrelevant to the wavelength scaling at the onset location, i.e. at the edge $r_0$ of the inner patch. This main conclusion of Zoueshtiagh & Thomas (2000) was based on the assumption that the critical wavelength $\lambda_0$ developing at the edge of the patch is independent of $r_0$. This assumption is equivalent to neglecting the centrifugal force. However, the assumption is not strictly valid as will be discussed in the following section.

## 7. Effect of centrifugal and Coriolis force

The effect of the centrifugal force is expected to be such that increasing centrifugal force lowers the effective threshold required for grain mobilization. For any particular fluid–granules combination, the critical threshold depends on the relative magnitudes of centrifugal force and gravitational force acting on the grains. When the centrifugal force is negligible in comparison to the gravitational force, then the assumption of Zoueshtiagh & Thomas (2000) that the grain-mobilization threshold is independent of the radial position holds. One then expects that the critical onset wavelength at the edge of the central granule patch is independent of the patch radius $r_0$. However, under otherwise constant conditions, the centrifugal force increases with radial position $r$. Thus, when it becomes of comparable magnitude to the gravitational force at any radius $r$, then the grain-mobilization threshold is expected to be lowered accordingly. The magnitude of the two forces for typical conditions encountered in our experiments can be estimated.

A typical value for the density of the grains used in many of the experiments in Thomas (1994) and Zoueshtiagh (2001) is of the order of $\rho_G \approx 2.65\ \mathrm{g\,cm^{-3}}$, the density of the fluid is typically $\rho_F = 1\ \mathrm{g\,cm^{-3}}$, the system rotates at maximum speeds around $\omega_1 = 5\ \mathrm{rad\,s^{-1}}$ and the inner patch radius is of the order of, say, half the tank radius and, hence, 25 cm. The centrifugal force per unit mass acting on the grains is $F_c = \rho_G \omega_1^2 r$. The gravitational force per unit mass is $F_g = \rho_G g'$ where $g' = g(\rho_G - \rho_F)/\rho_G$ is the reduced gravitational acceleration with $g$ representing the gravitational acceleration of the Earth. The ratio of the two forces is $F_c/F_g = \omega_1^2 r/g'$ and with the numeric values assumed above one determines $F_c/F_g \approx 1.02$. Hence, both forces can be of comparable magnitude and, consequently, one expects to observe a dependence of the onset wavelength $\lambda_0$ on the patch radius $r_0$.

The existence of the dependence of the ripple wavelength on the patch radius is confirmed by the experimental data shown in figure 5. These data pertain to the experiments summarized in Thomas (1994). The figure displays the onset wavelength $\lambda_0$ as a function of a Reynolds number defined as $Re = r_0 \Delta\omega l/\nu$, where $\nu$ is the kinematic viscosity of water and $l = (\nu/\Omega)^{1/2}$. In the expression for $l$, the quantity $\Omega$ is defined by Faller (1991) as

$$\Omega = \frac{\omega_0 + \omega_1}{4} + \left( \left( \frac{\omega_0 + \omega_1}{4} \right)^2 + \frac{(\omega_0 - \omega_1)^2}{2} \right)^{1/2}. \tag{7.1}$$

This definition summarizes Kármán flow ($\omega_0 = 0$, $\omega_1 \neq 0$), Bödewadt flow ($\omega_1 = 0$, $\omega_0 \neq 0$) and Ekman flow ($\omega_0 \approx \omega_1$) in one model. The velocities $\omega_0$, $\omega_1$ for the data displayed in figure 5 are in the range between 0 and $3.5\ \mathrm{rad\,s^{-1}}$.

Figure 5 reveals a linear dependence between the onset wavelength $\lambda_0$ and the Reynolds number $Re$. A least-squares fit interpolating the data points yields $\lambda_0 = 3.37 \times 10^{-4} Re + 3.13 \times 10^{-4}$. The constant $3.13 \times 10^{-4}$ is negligible in comparison to the term $3.37 \times 10^{-4} Re$ in the range of typical Reynolds numbers encountered in the experiment. Since the experimental conditions for the data in figure 5 are typical, it appears reasonable to conclude that $\lambda_0 \propto Re$.

At the edge of the patch one has to satisfy the condition that an integer number $n$ of wavelengths $\lambda_0$ fills the circumference of the central patch—this

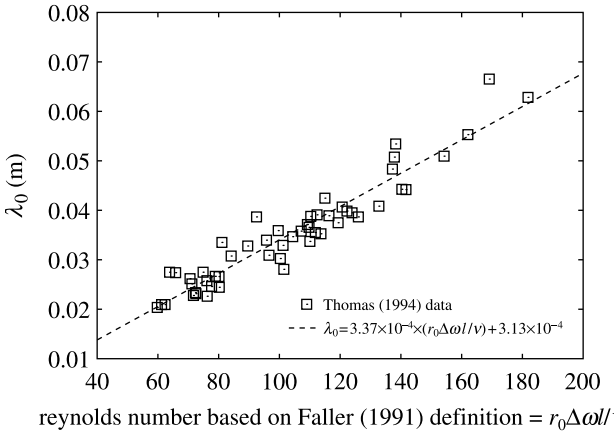


Figure 5. The wavelength $\lambda_0$ at the edge of the central granule patch as a function of the Reynolds number *Re*. The data pertain to the set of experiments summarized in Thomas (1994).

requirement translates into $n\lambda_0 = 2\pi r_0$. Solving the expression for $\lambda_0$ and introducing the result into $\lambda_0 \propto Re$ shows that $n \propto \Delta\omega^{-1}$. This is the same result obtained by Zoueshtiagh & Thomas (2000), who ignored the influence of the centrifugal force. Hence, while the centrifugal force acting on the grains will, of course, affect the absolute value of the wavelength $\lambda_0$, it will not affect the scaling of the ripple-wavelength with the velocity increment $\Delta\omega$ at pattern formation onset.

The second force arising from the background rotation of the system is the Coriolis force. This force only becomes effective, however, once the grains are in motion. Thus, it only acts after the system has selected its onset wavelength. Consequently, Coriolis forces associated with the motion of the grains cannot affect the wavelength scaling at onset.

## 8. Comparison of data for rotating and non-rotating systems

The experimental data obtained by Zoueshtiagh (2001) for the rotating system described in §2 are compared with comprehensive datasets for ripple formation in a number of different non-rotating systems in unidirectional (Coleman & Melville 1996; Betat 1999; Betat *et al.* 1999), as well as oscillatory (Manohar 1955; Sleath 1976; Scherer *et al.* 1999) flow. All data are from experiments where the ripples are observed to form within a few seconds. Thus, the data comparison is restricted to transitional ripples during the early stage of their evolution.

Data comparison is facilitated by non-dimensionalizing the ripple wavelength $\lambda$ using the grain diameter $d_G$ and displaying this ratio $\lambda/d_G$ as a function of a mobility parameter $\Theta$ defined as

$$\Theta = \frac{\rho_G U^2}{g(\rho_G - \rho_F)d_G} = \frac{U^2}{g' d_G}. \tag{8.1}$$

In equation (8.1), the quantity $U$ is a typical velocity scale characterizing the flow velocity above the granule layer and $g' = g(\rho_G - \rho_F)/\rho_G$ is the reduced

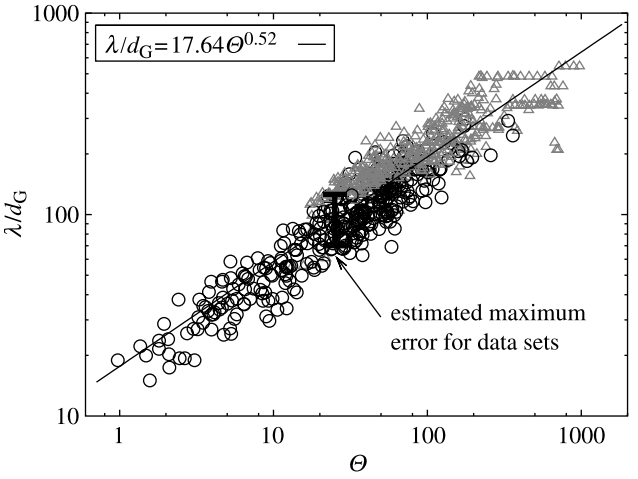


Figure 6. Non-dimensional ripple wavelength $\lambda/d_G$ as a function of the mobility parameter $\Theta$. Comparison of data from present experiments in a rotating system with data of other authors for ripple formation in non-rotating systems. Full references for the data used for comparison are included in main body of text.

gravitational acceleration acting on the grains. For our present system, this velocity is taken as $U=\Delta\omega r_0$. For details concerning the appropriate values of $U$, for the datasets from the non-rotating experiments used for comparison, consult Zoueshtiagh & Thomas (2003). Note that the mobility parameter $\Theta$ is similar to the Shields parameter or a Froude number. The mobility parameter $\Theta$ characterizes the ratio of the forces trying to mobilize the grains and the reduced gravitational force resisting grain mobilization.

The data comparison is shown in figure 6. The figure displays approximately 400 data points (circles) from our own experiments in the rotating system in comparison to around 500 data points (triangles) from the non-rotating experiments. Some of the latter experiments (Betat *et al.* 1999; Scherer *et al.* 1999) were carried out in a circular channel geometry with either a rotating flow over a granule layer at rest or an oscillating (moving) granular bed with a fluid at rest. Note, however, the crucial difference with regard to our new system is that none of these experiments were subject to an absolute background rotation corresponding to the $\omega_1$ in our new system. The data displayed in figure 6 cover approximate parameter ranges for particle size and density of $0.11\ \mathrm{mm}\leq d_G\leq 3.17\ \mathrm{mm}$ and $1.28\ \mathrm{g\,cm^{-3}}\leq\rho_G\leq 7.9\ \mathrm{g\,cm^{-3}}$, respectively.

Figure 6 reveals that the data points of all systems collapse on one line extending over three orders of magnitude along the abscissa and two orders of magnitude along the ordinate. A detailed comparison, which in particular illustrates the effect of the non-dimensionalization scheme on individual raw datasets, is contained in Zoueshtiagh & Thomas (2003).

The line interpolating the data in figure 6 represents a least-squares fit to all 900 data points. The data interpolation constitutes a linear fit of type $y=mx+b$ in the coordinates $y=\ln(\lambda/d_G)$ and $x=\ln(\Theta)$. The fitting routine yielded values of $m=0.52\pm0.01$ and $b=2.87\pm0.03$. This implies that $\lambda/d_G=17.64\Theta^{0.52}$. From this, one concludes $n\propto\Delta\omega^{-1.04}$, which confirms the scaling already revealed by figure 5 for the data of Thomas (1994). Hence, the analysis shows that the data

for the ripple patterns in our rotating system obey the same scaling one observes for sand ripples in non-rotating systems.

Note that the data interpolation of the data points in figure 5 implies $\lambda \propto d_{\mathrm{G}}^{0.48}$. This supports the results of Raudkivi (1997) and Bagnold (1946). For uniform flow, Raudkivi (1997) stated that the 'initial ripple length appears to be proportional to $\sqrt{d_{\mathrm{G}}}$', while for oscillatory flow, Bagnold reported that the wavelength 'varies nearly as the square root of the diameter'.

## 9. Summary and outlook

The main result expressed by figure 6, which is of relevance in the present context, is the collapse of the data for rotating and non-rotating systems on the same straight line. This indicates that background rotation does not affect the scaling of the ripple-wavelength with the independent experimental parameters. Consequently, it should be possible to utilise the rotating system to study aspects of ripple formation in non-rotating geophysical systems.

From a practical viewpoint, experiments employing our rotating system are substantially less labour intensive than traditional studies in water channels. In the rotating system, the effective azimuthal velocity $U$, which mediates ripple formation, increases with the distance from the centre of the tank. The velocity is $U=0$ in the centre of the tank at $r=0$ and it has maximum values of the order of $U=\Delta\omega R$ near the outer wall of the tank. If the analogy between rotating and non-rotating systems holds, then this may be viewed as a series of non-rotating experiments with different flow speeds being covered simultaneously by one single rotating experiment.

In particular, the new rotating system represents an easy means to determine the *shortest* wavelength that any particular granular material underlying a given fluid can display. Ripple formation in the rotating system is initiated at the edge of the central granule patch. There, the local conditions must necessarily equal the critical conditions required to mobilize the particles and initiate pattern formation. Consequently, the developing wavelength is always the smallest wavelength that can be established.

A further advantage of our new system is that it enables one to decrease the threshold for grain motion and, thus, for ripple formation. The threshold decrease is brought about by utilising the centrifugal force arising from the system rotation. Threshold control can be beneficial because it enables the study of ripple formation or grain motion below the natural threshold observed in water-channel experiments. The threshold decrease is reflected in figure 6 by the data from the present experiments extending to values of $\Theta$ which are more than one order of magnitude smaller than any of the data used for comparison. The values of $g'$ and $d_{\mathrm{G}}$ are constant for a fixed granule–fluid combination. Hence, reference to equation (8.1) shows that the critical velocity $U$ for grain mobilization must have been reduced in order to establish very low values of $\Theta$.

The threshold decrease can be interpreted as an effective decrease of gravitation. Assume, for instance, that the gravitational acceleration reduces from its value of $g=9.81\ \mathrm{m\,s^{-2}}$ on Earth to, say, $0.37\ g \approx 3.63\ \mathrm{m\,s^{-2}}$ on Mars. If particle and fluid density remain unchanged, then the value of $g'$ and, consequently, the grain mobilization-threshold will decrease accordingly.

Equation (8.1) shows that the critical forcing velocity $U$ required for grain mobilization must be lowered accordingly in order to achieve dynamic similarity. Therefore, our system may enable simulation of ripple formation on other planets.

Finally, our new system may provide the opportunity to gain some means of control over the boundary-layer thickness in the fluid above the granular layer and, thus, over the shear forces acting on the granules. In water channels, the boundary-layer thickness increases with the downstream flow direction. The thickness $\delta$ of the laminar boundary layer over a rotating surface, however, is independent of the distance from the axis of rotation. It is equal to $\delta = c(\nu/\Omega)^{1/2}$, where $\Omega$ is a function of $\omega_0$ and $\omega_1$ as defined in equation (7.1). The factor $c$ ranges between 5.5 for Kármán flow ($\omega_0 = 0$, $\omega_1 \neq 0$) and 8.5 for Bödewadt flow ($\omega_1 = 0$, $\omega_0 \neq 0$; Owen & Rogers 1989, ch. 3). We have recently measured that laminar-turbulent transition over a rough rotating disk—which is comparable to the surface of the granule layer—does not appear to be significantly influenced by roughness as long as this remains below a certain critical level (Zoueshtiagh *et al.* 2003).

If the number of spiral-ripple arms does not change for $r > r_0$, as is the case in figure 2, then the constraints imposed by the circular geometry evidently require that $\lambda(r) \propto r$. If the azimuthal velocity is of the order $U(r) = \Delta\omega r$, then it necessarily follows that $\lambda(r) \propto U(r)$. This result is expressed by the least-squares fit interpolating the data points in figure 6. The fit yielded $\lambda \propto \Theta^{0.52}$, which implies $\lambda \propto U^{1.04}$. Hence, the wavelength is proportional to the forcing of the system which is here expressed in terms of the flow velocity $U$ above the granular layer. This result is trivial for our rotating experiments where it simply arises from symmetry constraints. However, figure 6 implies that the same result also holds for the non-rotating experiments used for comparison—which are not subject to the geometric constraints encountered in the present system. While our data for the rotating systems are always associated with the smallest possible wavelength that the system can display, this is not so for the data used for comparison. There, the wavelength data are, generally, not associated with the critical onset condition and the measured wavelength is a function of the mediating flow velocity above the granule layer.

## References


Allen, J. R. L. 1984 *Sedimentary structures.* Amsterdam: Elsevier.

Bagnold, R. A. 1941 *The physics of blown sand and desert dunes.* London: Methuen.

Bagnold, R. A. 1946 Motion of waves in shallow water: interaction between waves and sand bottoms. *Proc. R. Soc. A* **187**, 1–18.

Betat, A. 1999 *Rippelbildung granularer Materie unter dem Einfluß einer Wasserscherströmung.* Ph.D. thesis, Otto-von-Guericke Universität, Magdeburg, Germany.

Betat, A., Frette, V. & Rehberg, I. 1999 Sand ripples induced by water shear flow in an annular channel. *Phys. Rev. Lett.* **83**, 88–91.

Blondeaux, P. 2001 Mechanics of coastal forms. *Annu. Rev. Fluid Mech.* **33**, 339–370.

Coleman, S. E. & Melville, B. W. 1996 Initiation of bed forms on a flat sand bed. *J. Hydrol. Eng.* **122**, 301–310.

Faller, A. J. 1991 Instability and transition of the disturbed flow over a rotating disk. *J. Fluid Mech.* **230**, 245–269.

Fryberger, S. G., Hesp, P. & Hastings, K. 1992 Aeolian granule ripple deposits, Namibia. *Sedimentology* **39**, 319–331.

Greeley, R. & Iversen, J. D. 1985 *Wind as a geological process*. Cambridge: Cambridge University Press.

Harms, J. C. 1969 Hydraulic significance of some sand ripples. *Geol. Soc. Am. Bull.* **80**, 363–395.

Kennedy, J.F. & Falcon, M. 1965 Wave generated sediment ripples. Hydrodynamics Laboratory Report no. 86, Department of Civil Engineering, Massachusetts Institute of Technology, MA, USA.

Lancaster, N. 1995 *Geomorphology of desert dunes*. London: Routledge.

Manohar, M. 1955 Mechanics of bottom sediment movement due to wave action. US Army, Beach Erosion Board Tech. Memo.

Nishimori, H. & Ouchi, N. 1993 Formation of ripple patterns and dunes by wind-blown sand. *Phys. Rev. Lett.* **71**, 197–200.

Owen, J. H. & Rogers, R. H. 1989 *Flow and heat transfer in rotating-disk systems. Rotor–stator systems*, vol. 1. Taunton, Somerset: Research Studies Press.

Raudkivi, A. J. 1990 *Loose boundary hydraulics*, 3rd edn. Oxford: Pergamon Press.

Raudkivi, A. J. 1997 Ripples on stream bed. *J. Hydrol. Eng.* **123**, 58–64.

Scherer, M., Melo, F. & Marder, M. 1999 Sand ripples in an oscillating annular sand–water cell. *Phys. Fluids* **11**, 58–67.

Sharp, R. P. 1963 Wind ripples. *J. Geol.* **71**, 617–636.

Sleath, J. F. A. 1976 On the rolling grain ripples. *J. Hydrol. Res.* **14**, 69–81.

Sleath, J. F. A. 1984 *Sea bed mechanics*. New York: Wiley.

Stegner, A. & Wesfreid, J. E. 1999 Dynamical evolution of sand ripples under water. *Phys. Rev. E* **60**, R3487–R3490.

Thomas, P. J. 1994 Pattern formation of granules on the bottom of a differentially rotating tank. *J. Fluid Mech.* **274**, 23–41.

Yalin, M. S. 1965 *Similarity in sediment transport by currents. Hydraulics research paper*, vol. 6. London: Ministry of Technology.

Zoueshtiagh, F. 2001 Experimental and computational study of spiral patterns in granular media underneath a rotating fluid. Ph.D. thesis, University of Warwick, Coventry, UK.

Zoueshtiagh, F. & Thomas, P. J. 2000 Wavelength scaling of spiral patterns formed by granular media underneath a rotating fluid. *Phys. Rev. E* **61**, 5588–5592.

Zoueshtiagh, F. & Thomas, P. J. 2003 Universal scaling for ripple formation in granular media. *Phys. Rev. E* **67**, 031301.

Zoueshtiagh, F., Ali, R., Colley, A. J., Thomas, P. J. & Carpenter, P. W. 2003 Laminar-turbulent boundary-layer transition over a rough rotating disk. *Phys. Fluids* **15**, 2441–2444.